Nucleon-induced inelastic cross sections on ^{nat}Ni

A. Olacel, C. Borcea, M. Boromiza, S. Calinescu, C. Clisu, C. Costache, Ph. Dessagne, I. Dinescu, D. Filipescu, N. Florea, et al.

Nucleon-induced inelastic cross sections on ^{nat}Ni

A. Olacel,[1] C. Borcea,[1] M. Boromiza,[1,*] S. Calinescu,[1] C. Clisu,[1] C. Costache,[1] Ph. Dessagne,[2] I. Dinescu,[1] D. Filipescu,[1] N. Florea,[1] I. Harca,[1] G. Henning,[2] A. Ionescu,[1] M. Kerveno,[2] R. Lica,[1] A. Matei,[1] C. Mihai,[1] R. Mihai,[1] A. Mitu,[1] A. Negret,[1] C. Nita,[1] M. Nyman,[3] A. Oprea,[1] C. Petrone,[1] A. J. M. Plompen,[3] C. Sotty,[1] L. Stan,[1] L. Stoica,[1,4] G. Suliman,[1,5] A. Turturica,[1] and S. Ujeniuc[1]

[1]*Horia Hulubei National Institute for Physics and Nuclear Engineering, Reactorului 30, 077125 Bucharest-Măgurele, Romania*
[2]*Université de Strasbourg, Centre National de la Recherche Scientifique, IPHC UMR 7178, F-67000 Strasbourg, France*
[3]*European Commission, Joint Research Centre, Retieseweg 111, B-2440 Geel, Belgium*
[4]*University of Bucharest, Faculty of Physics, Atomistilor 405, 077125 Bucharest-Măgurele, Romania*
[5]*Physics Department, University Politehnica of Bucharest, Splaiul Independentei Number 313, 060042 Bucharest-Sector 6, Romania*

(Received 8 June 2022; accepted 26 July 2022; published 17 August 2022)

This paper reports on the results of $(n, n'\gamma)$ and $(p, p'\gamma)$ cross section measurements on nickel performed at the Geel Electron Linear Accelerator of the European Commission, Joint Research Centre (Geel) and at the 9-MV Tandem Accelerator of Horia Hulubei National Institute for Physics and Nuclear Engineering (Bucharest-Magurele), respectively. The main goal was to reliably measure with small uncertainty the most intense transitions arising from the inelastic channel. Comparisons are performed between the extracted results, nuclear reaction model calculations using default parameter values, and previously reported measurements, if available. The broader goal of this paper is related to our study on the possibility of inferring neutron inelastic cross sections from the proton-induced ones, in this case for ^{58}Ni. We show that—by making use of the Lane consistency of the nucleon optical model potential and of the constraints offered by the proton data—one can extract a neutron-target potential that better describes the experimental data, as compared to the calculation with default neutron parameters. We also discuss relevant issues and still open questions of our calculations along with future plans for mitigation.

DOI: 10.1103/PhysRevC.106.024609

I. INTRODUCTION

Fossil-fuels-based energy production poses long term important ecological threats. Hence, for a sustainable development of our society, we need to progressively replace this type of energy production with improved, ideally far less polluting, technologies. Nuclear energy represents one such option if the current nuclear facilities are upgraded in terms of safety, economic efficiency/costs, availability of the nuclear fuel, danger of proliferation, etc. Within this context, there is an ongoing effort to develop new types of nuclear facilities: small modular reactors, generation IV fast reactors, accelerator driven systems (ADS), and others [1–8]. Such facilities will be able to burn much more abundant nuclear fuels (such as ^{238}U) while recycling part of the minor actinides resulting from neutron capture and/or decay of the primary fission products. From a practical point of view, measuring the neutron inelastic channel is motivated by the request of very precise and reliable cross section data for the development of these facilities. The precision required by the nuclear applications, typically under 5%, poses serious experimental difficulties. On the other hand, such precisely measured reaction observables can also be used for placing important constraints on both the nuclear reaction and structure models, leading to their improvement.

Inelastic scattering is the main neutron slowing down mechanism inside a reactor contributing to its reactivity. Consequently, this reaction plays an important role in reactor criticality, neutron transport, shielding, and other issues. It is therefore important to provide good quality inelastic cross sections in a large incident energy range (from the threshold up to around 20 MeV) for all the target nuclei of interest for the scientific community. This paper studies the nucleon inelastic channel on nickel, which is one of the components of heat- and corrosion-resistant Fe-Cr-Ni steel, a frequently used structural material in all nuclear facilities including the sodium-cooled fast reactors and the ADS facilities [1–8]. Natural nickel has five stable isotopes with ^{58}Ni [68.077(6)%] being the most abundant followed by ^{60}Ni [26.223(5)%], ^{62}Ni [3.634(1)%], ^{61}Ni [1.139(4)%], and ^{64}Ni [0.926(6)%] [9].

Our primary goal was to measure the γ-production cross sections of the most intense transitions. The extracted results are compared with previous experimental values, taken from the EXFOR (Exchange Format) database [10] and summarized in Table I, for the neutron experiment. For the neutron-induced transitions reported in the present paper, only the authors of Refs. [15,19] measured cross sections in an extended incident

*marian.boromiza@nipne.ro

TABLE I. Previously reported neutron-induced inelastic γ-production cross sections on nickel isotopes.

Reference	Year	Sample	E_n range (MeV)	Detectors	EXFOR entry
Bazavov *et al.* [11]	1971	^{58}Ni	1.9–3.0	GeLi	40736
Broder *et al.* [12]	1964	^{58,60}Ni	1.3–4.1	NaI	40139
Konobeevskii *et al.* [13]	1972	^{58,60}Ni	1.3–1.6	GeLi	40096
Tessler and Glickstein [14]	1975	^{60}Ni	3.4–5.4	GeLi	10439
Voss *et al.* [15]	1978	^{58,60}Ni	1.3–13.5	GeLi	20744
Nishimura *et al.* [16]	1965	^{58,60,64}Ni	0.3–2.6	NaI	
Traiforos *et al.* [17]	1979	^{58,60,62,64}Ni	1.5–4	GeLi	
Breunlich *et al.* [18]	1971	^{58,60}Ni	14.4	GeLi	21286
Fotiades *et al.* [19]	1979	^{60}Ni	1–250	GEANIE spectrometer	14359

energy range. Hence, we will mainly focus on the comparison between our results and those of Voss *et al.* [15] and Fotiades *et al.* [19]. For the proton experiment, there are no angle-integrated γ-production cross section data in an extended incident energy range on ^{58}Ni reported in the literature [10]. In the present paper we measured proton-induced cross sections for the first transition from 4 to 17 MeV with very small incident energy steps (25 keV). This allowed us to map out the CN resonances in ^{59}Cu. For the secondary transitions we report cross section points, with 1-MeV steps, up to 17 MeV (see Sec. IV).

Apart from measuring reliable and precise nucleon-induced inelastic cross sections, this paper also has a secondary, more exploratory, goal: to concomitantly investigate the neutron and the proton inelastic cross sections on the same nucleus with the purpose of finding a procedure able to relate the two quantities. The present investigation, dedicated to ^{58}Ni, is a direct continuation of our previous studies on ^{16}O and ^{28}Si [20–22]. The first study, dedicated to ^{28}Si [20], involved exploring an idea inspired by the *surrogate-reactions method* [23]. More precisely, Ref. [20] studied the possibility of inferring the neutron-induced inelastic γ-production cross sections on ^{28}Si from those extracted measuring the ^{25}Mg$(\alpha, n)^{28}$Si reaction. The two reactions proceed through the same CN and have identical exit channels. Hence, in a naive interpretation of the Bohr hypothesis for the CN reactions [24], one could expect similar inelastic cross sections in the two cases. The main conclusion of Ref. [20] was however that, even though the two cross sections have proportional values at relatively high incident energies where the Coulomb-barrier effects are small, a direct comparison yields differences as large as 80%. This can be understood considering the relatively big differences between the optical model potentials (OMPs) describing the $(n, ^{28}$Si) versus $(\alpha, ^{25}$Mg) projectile-target combinations, such as no Coulomb term for the incident neutron, different projectile and ground state spins of the two targets, and, hence, relatively large differences between the total angular momentum populated in the CN.

Numerous studies were performed within the surrogate approach [23,25–31] yielding encouraging results in a few particular cases: neutron capture, fission, and, recently, also the (n, p) channel [32]. The surrogate method generates the nucleus of interest that undergoes fission or γ decay through a direct reaction induced by a high-energy charged particle. Even though our approach is different than the surrogate method, the broader goal of the present paper is somewhat similar: to find a general procedure able to infer the neutron inelastic cross sections of interest from charged particle-induced reactions.

In our previous studies [21,22] mentioned above, in order to increase the similarities between the projectile OMPs, we made use of the isospin symmetry in mirror nuclei by employing $N = Z$ targets. More precisely, we measured neutron- and proton-induced inelastic reactions on ^{16}O and ^{28}Si [21,22]. Isospin symmetry generates well-known structural similarities between mirror nuclei. This fact, coupled with the great formal and parametrization similarities between the neutron and proton OMPs on the same target, generates comparable (or even proportional) inelastic γ-production cross sections [22]. Starting from the experimental proton-induced inelastic data and following the procedure described in Ref. [22], we showed that it is possible to relate (with around 10% precision) the neutron and proton inelastic channels on ^{16}O and ^{28}Si.

In the present paper we use Lane-consistent neutron and proton OMPs [33–35]. For the two nucleons, this type of potential has a formally identical Lane term, which is proportional to $(N - Z)/A$, but with a different sign [22,35]. This term is zero in case of ^{16}O and ^{28}Si. The present study on ^{58}Ni has therefore a twofold purpose: to further improve on the issues of the procedure described in Ref. [22] aiming to relate the proton and neutron inelastic channels and to investigate the effects on this procedure of a nonzero Lane term [33,34]. Because ^{58}Ni has two extra neutrons as compared to protons, the two compound nuclei ^{59}Ni and ^{59}Cu through which the neutron- and proton-induced reactions proceed are not mirror nuclei anymore. This fact could generate larger nuclear structure-related differences between the neutron and proton reactions. Section V discusses these and other issues in detail.

II. THE EXPERIMENTAL SETUPS USED IN THE TWO EXPERIMENTS

A. The GELINA neutron source of EC-JRC and the GAINS spectrometer

The neutron-induced data reported in this paper were measured at the Geel Electron Linear Accelerator (GELINA)

neutron source [36]. The γ rays of interest coming from the inelastic channel were detected using the Gamma Array for Inelastic Neutron Scattering (GAINS) spectrometer [37]. The latter was read out by 420-MHz 12-bit ACQIRIS digitizers [38]. GELINA is a high-resolution, pulsed neutron source. The time-of-flight technique and a fission chamber (FC) [39] are used to determine the incident energy and neutron flux, respectively. Details on this facility and on the detection system are given in Refs. [40,41]. For the present experiment we made use of a 100-m flight path and a 2.661(21)-mg/cm^2 natural nickel target with a diameter of 8.23(3) cm. It was irradiated for a total of $\approx$ 15 days (after data selection) allowing us to gain good statistics for the most intense transitions.

B. The 9-MV tandem accelerator of IFIN-HH and the HPGe detection system

The proton-induced experiment was performed at the 9-MV Tandem facility of the Horia Hulubei National Institute for Physics and Nuclear Engineering (IFIN-HH), Bucharest-Măgurele [42,43]. The incident protons had energies ranging from 4 to 17 MeV and they were scattered by two ^{58}Ni enriched targets of 0.30(3) and 6.43(6) mg/cm^2. We employed either 25-keV (the thin target) or 1-MeV (the thick target) incident energy steps to construct the excitation functions. A Faraday cup with a length of 30 cm, with a diameter of 2 cm, and placed around 7 cm after the ^{58}Ni target was used to integrate the beam current. For γ ray detection we used two HPGe detectors with 100% relative efficiency placed at 150° and 110° relative to the proton beam direction and at around 16 cm from the target. For data taking we used a digital acquisition: FASTER cards with a 125-MHz sampling frequency and 14 bits for amplitude resolution [44]. The FPGA board of the digitizer analyses the sampled signals online, hence avoiding their transfer to the PC for the extraction of the time and amplitude information. This feature allowed us to measure even at relatively high counting rates. The latter, however, generated dead time losses for which we corrected using the method presented in Refs. [45,46].

III. DATA ANALYSIS PROCEDURE

A. The neutron beam experiment

The data analysis procedure associated with our experiments at the GELINA neutron source using the GAINS spectrometer is described elsewhere [21,22,40,41,47,48]. For each observed transition, we first determine the differential γ-production cross section at 110° and 150° using the expression

$$\frac{d\sigma_j}{d\Omega}(\theta_i, E_n) = \frac{1}{4\pi} \times \frac{Y_j(E_n)}{Y_{\rm FC}(E_n)} \times \frac{\varepsilon_{\rm FC}}{\varepsilon_j(E_\gamma)} \times \frac{\rho_U}{\rho_s} \times \frac{A_s}{A_U} \times \frac{\sigma_U(E_n)}{c_{\rm MS}(E_n)} \tag{1}$$

where θ_i is the detection angle, E_n is the incident neutron energy, E_γ is the γ energy, Y_j is the number of counts measured by the detector j for a given γ line, $Y_{\rm FC}$ is the fission chamber yield, $\varepsilon_{\rm FC}$ is the fission chamber efficiency, $\varepsilon_j(E_\gamma)$ is the photopeak efficiency of the detector j, $\sigma_U(E_n)$ is the ^{235}U(n, fission) cross section [49], ρ_U is the areal density of the uranium deposits from the FC, A_U and A_s are the ^{235}U and sample atomic masses, ρ_s is the areal density of the sample corresponding to the isotope A_s (we used a natural nickel target), and $c_{\rm MS}$ is the neutron multiple scattering correction factor.

The chosen detection angles allow us to precisely angularly integrate the cross section by making use of the Gaussian quadrature method [21,48,50]:

$$\sigma(E_n) = 4\pi \left[w_{110^\circ} \frac{d\sigma}{d\Omega}(110^\circ, E_n) + w_{150^\circ} \frac{d\sigma}{d\Omega}(150^\circ, E_n) \right] \tag{2}$$

where $\frac{d\sigma}{d\Omega}(110^\circ, E_n)$ and $\frac{d\sigma}{d\Omega}(150^\circ, E_n)$ are the above differential cross sections at 110° and 150°, respectively. The normalization coefficients $w_{110^\circ} = 0.652\,14$ and $w_{150^\circ} = 0.347\,86$ are calculated by solving the system of equations resulting from a series expansion of the differential cross section in the Legendre polynomials basis [21,48,50].

B. The proton beam experiment

For measuring the proton-induced inelastic cross sections we used similar γ-spectroscopy techniques to the ones associated with the neutron beam experiment. One important difference is given by the fact that we extracted absolute cross sections using a Faraday cup to integrate the proton beam current. First, we constructed the amplitude spectra for each detector and incident proton energy. The γ peaks coming from ^{58}Ni were then identified and integrated. The differential cross sections at 110° and 150° were determined using the expression

$$\frac{d\sigma_j}{d\Omega}(\theta_i, E_p) = \frac{1}{4\pi} \times \frac{N_\gamma(\theta_i, E_p) A_s}{N_p(E_p)\varepsilon_j(E_\gamma)\rho_s} \times d \tag{3}$$

where θ_i is the detection angle, E_p is the incident proton energy, E_γ is the γ energy, N_γ is the integrated number of counts from a particular γ peak, N_p is the number of protons incident on the target, $\varepsilon_j(E_\gamma)$ is the photopeak efficiency of detector j, A_s is the atomic mass, ρ_s is the target areal density, and, finally, d is the dead time correction factor. The latter was calculated using the method presented in Refs. [45,46], as mentioned in the previous section.

To angularly integrate these differential cross sections we employed the same expression as for the neutron-induced experiment [i.e., relation (2)] considering that the detection angles are the same. For other details of the data analysis procedure associated with our proton beam experiments at IFIN-HH see Refs. [21,51].

IV. EXPERIMENTAL RESULTS

This section presents the results of the two experiments: we will start with the neutron (Sec. IV A) followed by the proton data (Sec. IV B). We were able to measure in total the γ-production cross section for 14 transitions associated with several nickel isotopes. Section IV C discusses the sources of uncertainty.

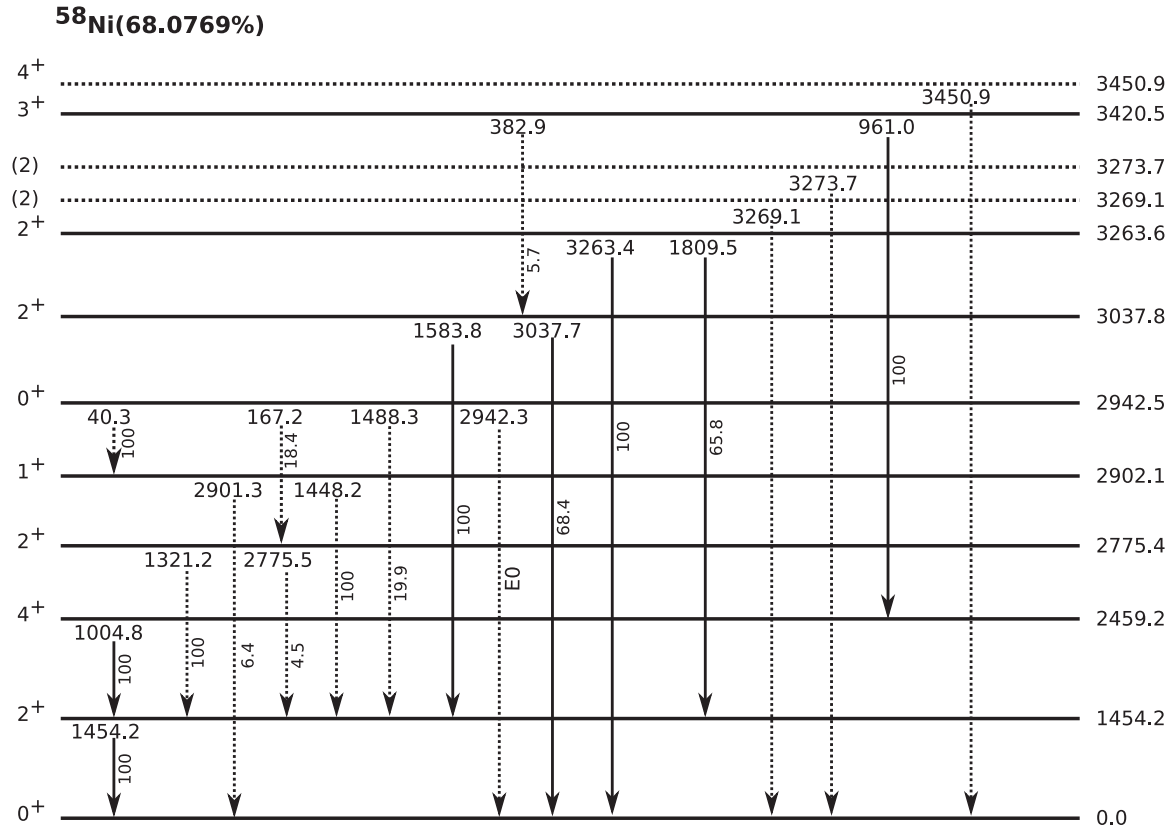

FIG. 1. A partial level scheme of ^{58}Ni. In the present paper we were able to extract the neutron-induced cross section for the transitions plotted with a continuous line. The level and γ energies are given in keV.

The ^{58}Ni target nucleus has a 0^+ ground state followed by a 2^+ first excited state (see Fig. 1). The 2^+ decays through a relatively intense 1454.2-keV transition. The second level, 4^+, deexcites through a 1004.8-keV γ ray [52]. These two transitions take up most of the inelastic strength. The 1321.2- and 1448.2-keV transitions—coming from the third and fourth excited levels, respectively—are important γ rays for which, unfortunately, we were not able to extract a clean cross section in the neutron-induced experiment. This was due to partial overlapping with close γ lines coming from the other nickel isotopes: the 1332.5- and 1454.2-keV peaks in ^{60}Ni and ^{58}Ni, respectively. We were able however to measure the production cross section for the 1321.2-keV transition in the proton-induced experiment. It is reported in Sec. IV B 2. The natural nickel target allowed us to observe transitions coming also from the secondary isotopes: 1332.5, 2158.6, and 952.4 keV from ^{60}Ni (see Fig. 2) and the main transition at 1345.7 keV from ^{64}Ni. Because the target contains only trace amounts of ^{59}Ni (unstable but with a relatively long half-life [52]), the ^{59}Ni$(n, 2n\gamma)^{58}$Ni polluting contributions to the γ-production cross sections of the ^{58}Ni transitions are negligible. However, this is not the case for the other stable isotopes of nickel which have non-negligible $(n, 2n)$ contributions.

We mention that, unfortunately, we were not able to construct relevant level cross sections as we could not detect and/or measure a clean cross section for the transitions feeding the excited levels of interest. Therefore, we will not report here level or total inelastic cross sections.

A. Neutron-induced γ-production cross sections

This subsection presents the results extracted in the neutron beam experiment performed at the GELINA neutron source. We report here the γ-production cross sections for several transitions coming from the stable nickel isotopes compared with theoretical calculations and other experimental data, when available.

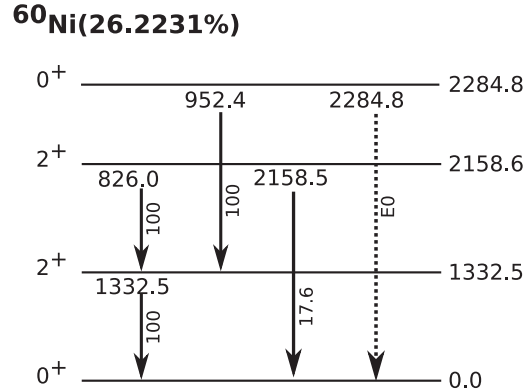

FIG. 2. A partial level scheme of ^{60}Ni. In the present paper we were able to extract the neutron-induced cross section for the transitions plotted with a continuous line. The level and γ energies are given in keV.

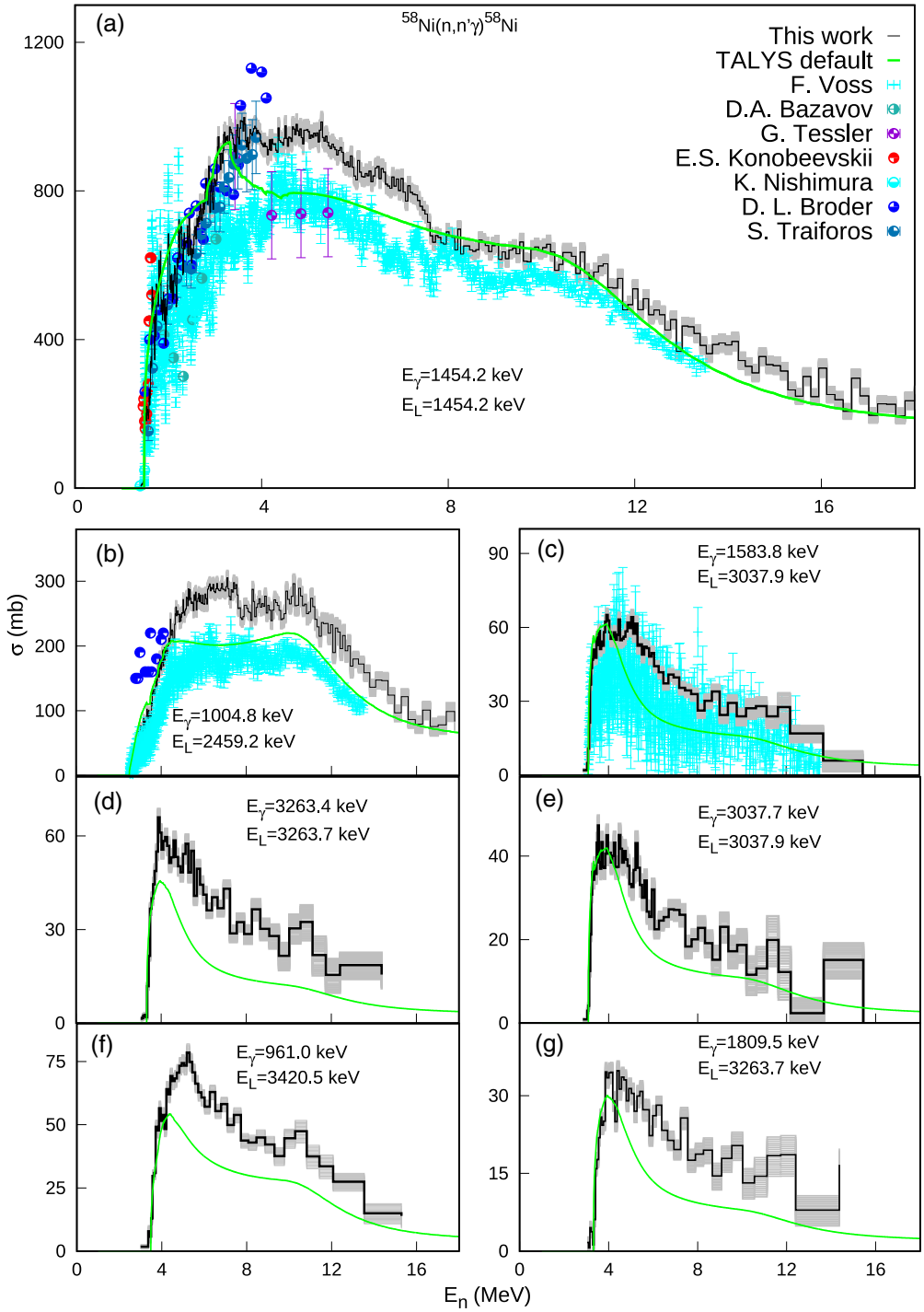

FIG. 3. The neutron-induced inelastic γ-production cross section for the transitions in ^{58}Ni reported in the present paper along with other experimental data, where available, and TALYS 1.9 default reaction calculations.

1. The main transition in ^{58}Ni: 1454.2 keV

Figure 3(a) displays the inelastic γ-production cross section for the main transition in ^{58}Ni. There are several previously reported results, with the most extended data set provided by Voss *et al.* [15]. The authors measured several γ rays coming from ^{58}Ni with good incident energy resolution up to about 14 MeV. The agreement with the present data is very good in terms of cross section trend but with a difference of around 20–25% in absolute values. This is also the case for the other ^{58}Ni and even ^{60}Ni transitions (see the next subsections). Interestingly, the same 20% difference was also observed for two other experiments that reported inelastic cross sections on ^{52}Cr and ^{238}U [15,47,48,53] (see also Fig. 3 of Ref. [54]). Voss *et al.* [15] measured ^{52}Cr using the same setup and data analysis procedure as the ones for

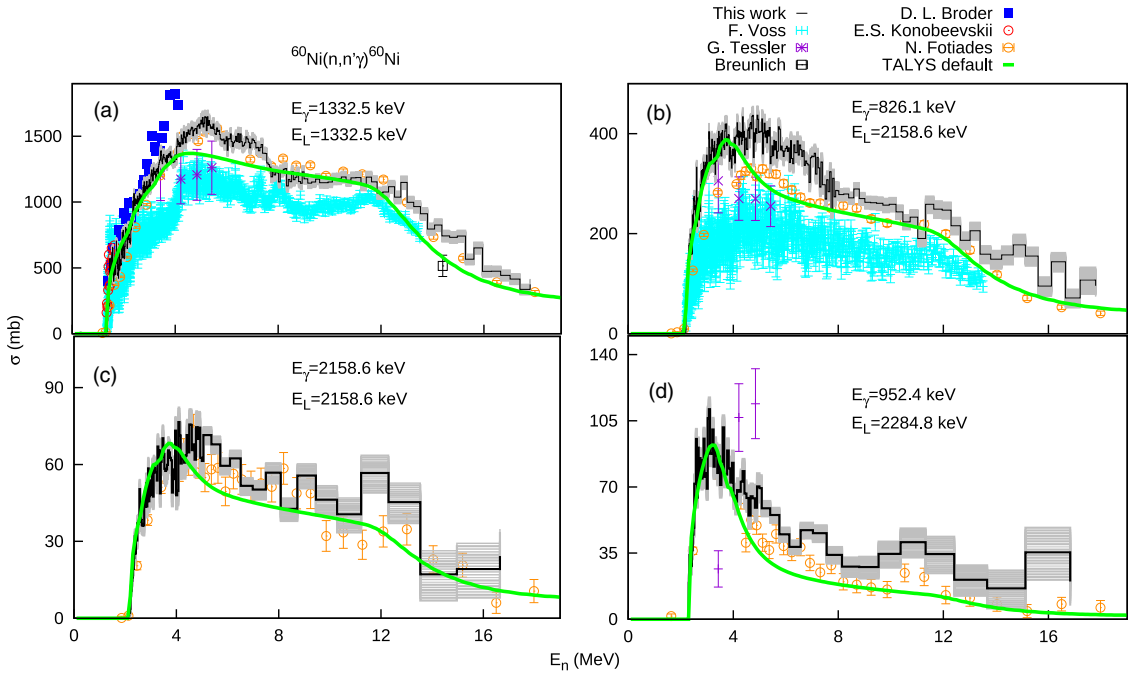

FIG. 4. The neutron-induced inelastic γ-production cross section for the most intense transitions in ^{60}Ni reported in the present paper along with other experimental data, where available, and TALYS 1.9 default reaction calculations.

^{58}Ni and ^{60}Ni, while the Mihailescu *et al.* [47,48] and Kerveno *et al.* [53] experiments were performed at GELINA using a similar HPGe-based setup and data analysis procedure to the ones employed in the present paper. The three data points reported by Tessler and Glickstein [14] are very close to the Voss *et al.* [15] values in the 4–6-MeV incident energy region while the agreement between our data and the other available experimental values shown in Fig. 3 is fairly good even though Bazavov *et al.* [11], Konobeevskii *et al.* [13], Nishimura *et al.* [16], Broder *et al.* [12], and Traiforos *et al.* [17] only reported cross section points close to the threshold region, below 4 MeV.

We report the inelastic cross section for the production of the most intense transition in ^{58}Ni with a total relative uncertainty ranging from around 5% at 5 MeV, where the cross section reaches its maximum value, to 10–12% at 18 MeV where the statistical component of the uncertainty dominates due to the low incident neutron flux and smaller cross section values. The theoretical curve, produced using the TALYS 1.9 reaction code with the default settings [35], is able to describe well our cross section values except for the 3–8-MeV region where the experimental data are underestimated, as shown in Fig. 3. The same disagreement can also be observed for the secondary transitions in ^{58}Ni, and even for ^{60}Ni (see Figs. 3 and 4).

2. *The secondary transitions in ^{58}Ni: 1004.8, 1583.8, 3263.4, 3037.7, 961.0, and 1809.5 keV*

Figures 3(b)–3(g) show the neutron-induced inelastic γ-production cross sections for the secondary transitions in ^{58}Ni. We were able to extract a clean cross section for six γ rays: 1004.8, 1583.8, 3263.4, 3037.7, 961.0, and 1809.5 keV. The 1004.8-keV γ ray is much more intense than the others with a maximum cross section reaching a plateau at 250 mb. Unfortunately, this plateau region from 4 to 12 MeV is where TALYS greatly underestimates our experimental values [see Fig. 3(b)]. For the other transitions the theoretical calculation underestimates also the high energy region. This difference is too large to be explained solely by missing higher-lying feeding associated with the excited levels which decay through these γ rays and thus it indicates in fact a poor neutron OMP for ^{58}Ni. This is also the case for ^{60}Ni, as discussed below.

Voss *et al.* [15] also reported cross section values for the 1004.8- and 1583.8-keV transitions in ^{58}Ni, but their data display the same normalization issues as for the main transition [see Figs. 3(b) and 3(c)]. The data of Broder *et al.* [12] were measured in a very narrow incident energy range; therefore, it is not conclusive for this comparison [see Fig. 3(b)]. For the other higher-lying transitions no other experimental data are available in the literature, so they are only compared with default theoretical calculation [see Figs. 3(d)–3(g)]. We report the cross section for the 1004.8-keV transition with comparable total relative uncertainties to the ones associated with the main transition whereas for the other higher-lying γ rays the uncertainties are considerably larger: 10–45% where the statistics are rather poor.

3. *The transitions in ^{60}Ni: 1332.5, 826.1, 2158.6, and 952.4 keV*

As mentioned in the previous sections, in the neutron beam experiment we used a natural target. This allowed us to extend the measurement to transitions coming from other nickel isotopes. In the case of ^{60}Ni we were able to extract clean production cross sections for three γ rays:

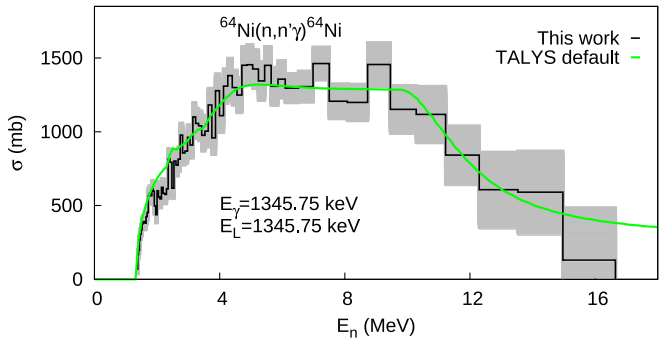

FIG. 5. The neutron-induced inelastic γ-production cross section for the main transition in ^{64}Ni reported in the present paper compared to TALYS 1.9 default reaction calculations.

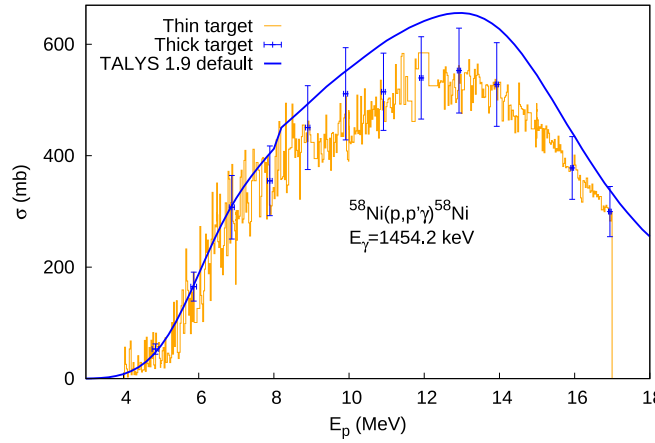

FIG. 6. The proton-induced inelastic γ-production cross section for the main transition in ^{58}Ni reported in the present paper compared to TALYS 1.9 default reaction calculations. For this transition we report data measured with two targets: 0.30(3) and 6.43(6) mg/cm^2. The cross section points associated with the thick target were extracted with 1-MeV incident energy steps and we measured the 6-, 7-, 8-, 9-, 10-, and 14-MeV incident energies several times to obtain a more reasonable assessment of our uncertainty spread (the plotted values for these incident energies were averaged). The thin target measurement employed very small 25-keV steps to map out the CN resonances.

1332.5, 2158.6, and 952.4 keV (see Fig. 4). The 826.1-keV γ ray is a relatively intense transition which displays systematically larger values than both the theoretical curve and other experimental results (see the same figure). It, unfortunately, was detected on top of a Germanium "triangle" caused by the inelastic scattering of neutrons on ^{72}Ge. Our background subtraction procedures may have been deficient in this case.

The main transition, shown in Fig. 4(a), is very intense with a maximum cross section value of 1500 mb. It compares very well with the data reported by Fotiades *et al.* [19] while the same normalization issue can be seen for the Voss *et al.* [15] values. The latter authors only reported values for the 1332.5- and 826.4-keV transitions. For the main transition, Konobeevskii *et al.* [13] and Broder *et al.* [12] are also in a very good agreement with the present paper even though the latter display larger values in the 3–4-MeV region [see Fig. 4(a)]. For the secondary transitions, shown in Figs. 4(c) and 4(d), the agreement between our data and the ones of Fotiades *et al.* [19] remains very good, with our data displaying slightly larger values at very high incident energies. The typical total relative uncertainties associated with the ^{60}Ni transitions range between 7 and 40%.

Even though in this case TALYS describes the experimental data better, as compared to ^{58}Ni discussed above, the same behavior is observed across transitions: good description of the threshold region followed by a relatively large underestimation at intermediate and high incident energies (see Fig. 4). This suggests that the differences seen in Figs. 3 and 4 for ^{58}Ni and ^{60}Ni are likely related to poor neutron OMPs for these two isotopes. The code, however, is able to describe very well the main transition in ^{64}Ni (see Fig. 5).

4. The main transition in ^{64}Ni: 1345.7 keV

Figure 5 shows the neutron-induced inelastic γ-production cross section for the main transition in ^{64}Ni. We compare our results only with theoretical calculations because no other data for angle-integrated inelastic γ-production cross section for the first transition exist. As already mentioned above, the neutron-^{64}Ni default optical potential implemented by TALYS 1.9 is able to model very well our experimental data in the entire incident energy range. Unfortunately, we did not detect any other γ rays coming from this nucleus as it would have been very useful for comparison with the theoretical calculations. Due to the relatively small natural abundance of ^{64}Ni, we could not collect very good statistics for the main transition. In consequence, the cross section points displayed in Fig. 5 have a total relative uncertainty ranging from 10 to 55%.

Moreover, we mention that, to cross-check the neutron-induced data, we also measured the γ-production cross section for the first transition in ^{28}Si, at 1778.9 keV. It compares very well with a previous experiment of our group that made use of a similar experimental setup, the same ^{28}Si target and an identical data analysis procedure [20]. This shows to some extent the reliability of the cross sections measured by our group at the GELINA neutron source.

B. Proton-induced γ-production cross sections

In the proton beam experiment we only measured the inelastic channel on ^{58}Ni using enriched targets, as compared to the neutron-induced measurement where data on several nickel isotopes could be extracted. This section presents these results and discusses comparisons only with theoretical calculations considering that, as already mentioned in the Introduction, no other proton-induced experimental values for angularly integrated inelastic γ-production cross sections exist for this target nucleus.

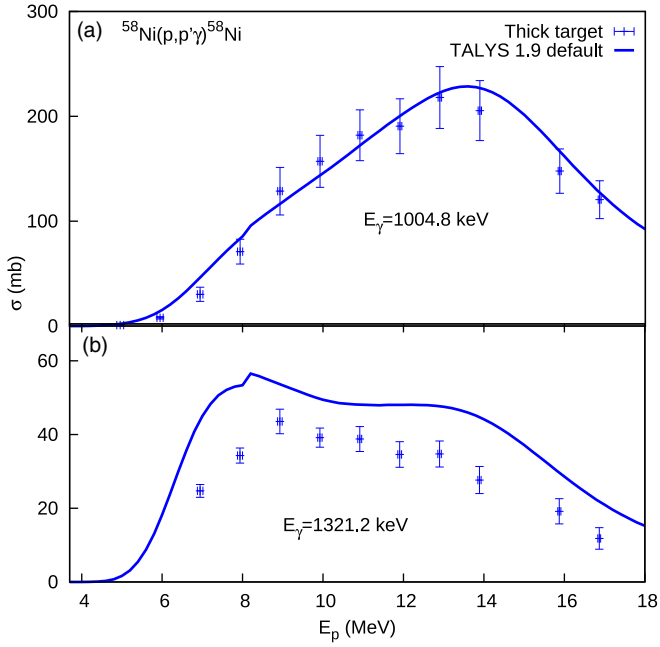

FIG. 7. The proton-induced inelastic γ-production cross sections for the (a) 1004.8- and (b) 1321.2-keV transitions in ^{58}Ni reported in the present paper compared to TALYS 1.9 default reaction calculations.

1. The main transition in ^{58}Ni: 1454.2 keV

Figure 6 displays our results for the main transition in ^{58}Ni. The reason for measuring using two targets with very different thicknesses was twofold: to gain additional confidence in our results (as the two measurements overlap) and to map out the CN resonances in ^{59}Cu using the thin target data.

The energy loss of 5-MeV protons is around 80 and 4 keV for the thick and thin targets, respectively. This energy loss translates into incident energy uncertainty that is relatively small and it was quantified by assuming a constant stopping power over the thickness of the target as even the lowest energy protons are far away from the Bragg total absorption peak (we employed a uniform distribution for calculating the average proton energy and its uncertainty after exiting the target [22]). In terms of the cross section uncertainty, it ranged from around 2 to 20% even though this intense transition allowed us to gain very good statistics at all incident energies. This relatively large uncertainty was caused—for those runs that were measured at (very) high counting rates—by the dead time correction factor, as explained in more detail in Refs. [21,45,46]. The theoretical curve provided by TALYS is in good agreement with our experimental points with a small contribution in the entire region above 7 MeV.

2. The secondary transitions in ^{58}Ni: 1004.8 and 1321.2 keV

Figure 7 shows the results for the other two transitions in ^{58}Ni: 1004.8 and 1321.2 keV. When compared to reaction calculations using the default settings, the TALYS curve describes well the experimental data associated with the first transition. In the case of the 1321.2-keV γ ray, the code's output overestimates the absolute values even though the shape of the cross section is well reproduced. Due to reduced statistics, we could not extract the cross section points for the 1321.3-keV γ ray at the 5- and 6-MeV incident energies as these points would have been helpful to better characterize the near threshold region. Overall, the proton optical model potential seems to provide a better modeling of the inelastic γ-production cross sections on ^{58}Ni as compared to the neutron-induced case (see Sec. IV A).

TABLE II. Sources of uncertainty and their associated values in the present neutron-induced experiment.

Source	Relative uncertainty (%)
Efficiency of the HPGe detectors	2–4
Efficiency of the fission chamber	2.1
Fission cross section of ^{235}U	<1
Areal density of the sample	1
Thickness of the fission chamber deposits	<1
Multiple scattering correction factor	<1

C. Uncertainty discussion

We report high precision inelastic data; hence, it is relevant to discuss in detail the uncertainties associated with the two experiments.

In the neutron-induced measurement, the main sources of uncertainty were the detected number of counts associated with a given γ line (4% for the main transition), the fission chamber yield (3%), and its efficiency (2.1%). Because we employed MCNP6 [55] simulations for extrapolating the efficiency of the detectors to high γ energies, the code provided a very small statistical uncertainty (below 0.5%). However, we know the activity of our ^{152}Eu calibration source within a 1.5% relative uncertainty. Therefore, the MCNP6 relative uncertainty was increased to 2%. This also accounts for any potential geometrical effects in the calibration source-detector position. The mass and area of the sample were measured accurately (1% areal density uncertainty). The sample and the ^{235}U deposits of the fission chamber had diameters larger than the neutron beam. In this way, any effects generated by nonuniformities in the beam profile were avoided.

The uncertainty associated with the multiple scattering coefficient and the self-attenuation of the γ rays inside the sample were quantified based only on Monte Carlo simulations, which yielded <1% values. We constructed the simulated detection geometry as realistically as possible and we validated it through comparisons to the ^{152}Eu experimental efficiency points. This fact allowed us to reasonably keep under control any potential systematic errors. Table II lists an overview of the uncertainties associated with the neutron beam experiment.

In the proton-induced experiment the relative uncertainty of the ^{152}Eu source was added to the statistical uncertainty arising from the MCNP6 simulations [55], giving a total of 3% for the detector efficiencies, ε_j. Given its geometrical characteristics (see Sec. II B) and its high efficiency, any charge loss from the Faraday cup is very small. Consequently, the uncertainty resulting from the integration of the proton beam (the

quantity N_p) was set to 1%. As mentioned, Refs. [21,45,46] explain how we quantify the uncertainty of the dead time correction factor, d. Depending on the run/counting rate, the latter had values ranging between 2 and 20%. We measured the target thickness using two independent methods: by weighting the target and measuring its area using a DinoLite Optic 2.0 laser device, and by α scattering using a ^{241}Am calibration source. Both methods agreed within the uncertainty bars with the α scattering resulting in larger uncertainties. Consequently, we chose to use the values provided by the first method which yielded a 1% uncertainty for the areal density, ρ_s. Other sources of uncertainty were given by the γ peak area, N_γ (between 3 and 5%, depending on the available statistics). We neglected the uncertainty coming from the atomic mass, A_s.

V. COMPARISON OF THE NEUTRON VERSUS PROTON REACTION DATA

This section continues our previous studies dedicated to ^{16}O and ^{28}Si [20–22]. As before, we focus on a nuclear reaction which allows us to infer, employing also theoretical input, the neutron-induced cross section data of interest by studying a simpler-to-measure case.

One way to make the two compared reactions more similar is to use *identical* CN so that the differences related to the *nuclear structure component* would be smaller. Such an investigation was performed in Ref. [20], but this type of approach yields very limited results when applied to the inelastic channel [21,22]. Another approach to this problem is given below and it consists in maximizing the *nuclear reaction component* similarities by using very similar optical potentials in the two compared reactions. We chose a proton-induced reaction on ^{58}Ni and we used proton OMPs, suitably constrained by proton-induced experimental cross sections, to infer the corresponding neutron inelastic cross sections.

Figure 8 shows a comparison between the neutron- and proton-induced inelastic γ-production cross section for the main three transitions in ^{58}Ni and TALYS 1.9 default calculations. The Coulomb barrier for incident protons induces much smaller inelastic cross sections at low energies, as compared to the neutron case. At high incident energies, the neutron and proton cross sections become more similar (proportional). In the following we discuss in more detail the reasons for the observed similarities (and differences) between the neutron- and proton-induced inelastic cross sections in the context of our attempt to relate the two quantities.

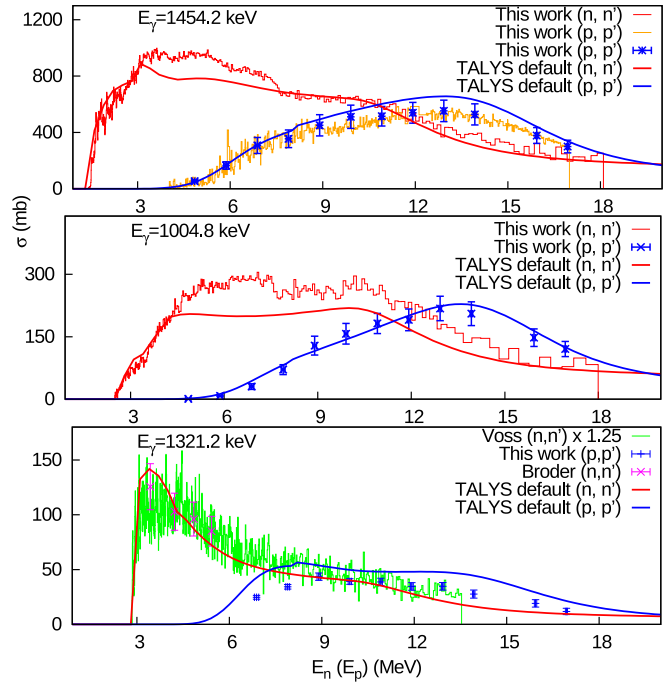

FIG. 8. The comparison between the neutron- and proton-induced inelastic γ-production cross section for three ^{58}Ni transitions and the corresponding TALYS 1.9 default calculations. For completeness, we display here also the Voss *et al.* data [15] for the 1321.2-keV transition as, unfortunately, we were able to extract clean cross sections in *both* experiments only for the two main transitions: 1454.2 and 1004.8 keV (see Sec. IV for details). Because in the same section of the paper we point out that the Voss *et al.* data are consistently lower by 20–25% than our results, their values plotted here—and in the next figures—were multiplied by 1.25.

A. General considerations: Nuclear structure and reaction ingredients

The present paper investigates nucleon-induced reactions on ^{58}Ni. This nucleus has $Z = 28$ and $N = 30$, with just two extra neutrons outside of the proton-closed $1f_{7/2}$ shell, which translates into a (nearly) spherical ground state and a typical example of a vibrational nucleus [56,57]. To model reactions on ^{58}Ni we employed spherical neutron and proton OMPs coupled with nuclear structure (collective) models to describe the deformation of several excited states, as detailed in the TALYS 1.9 User Manual [35]. The code offers two main options: the standard optical model, phenomenological, and a semimicroscopical approach which employs the so-called Jeukenne-Lejeune-Mahaux (JLM) optical potential. The mathematical formulation and parametrization for these potentials are extensively discussed in Refs. [33–35,58].

The JLM potential currently implemented in TALYS 1.9 is explicitly constructed in a Lane-consistent manner, that is, the parametrization and the energy dependence of the potential depth normalization factors are identical in the neutron and proton cases (see Sec. III.A of Ref. [58]). This is not the case for the phenomenological (default) OMP used by this reaction code even though the parametrizations for the two nucleons and the Lane/asymmetry term are very similar (see Sec. 4.1.1 of the TALYS 1.9 User Manual [35]).

There are several factors driving the differences between the neutron and proton reactions on ^{58}Ni.

(1) Coulomb barrier-driven: this plays the dominant role (see Figs. 9–11).

(2) At the same incident energy, the neutron always populates CN excited states that are 5580.6 keV higher than the corresponding proton reaction; this is due to the neutron and proton separation energy difference in the two CN through which the reactions proceed [52]—$S_n(^{59}\text{Ni}) - S_p(^{59}\text{Cu}) =$

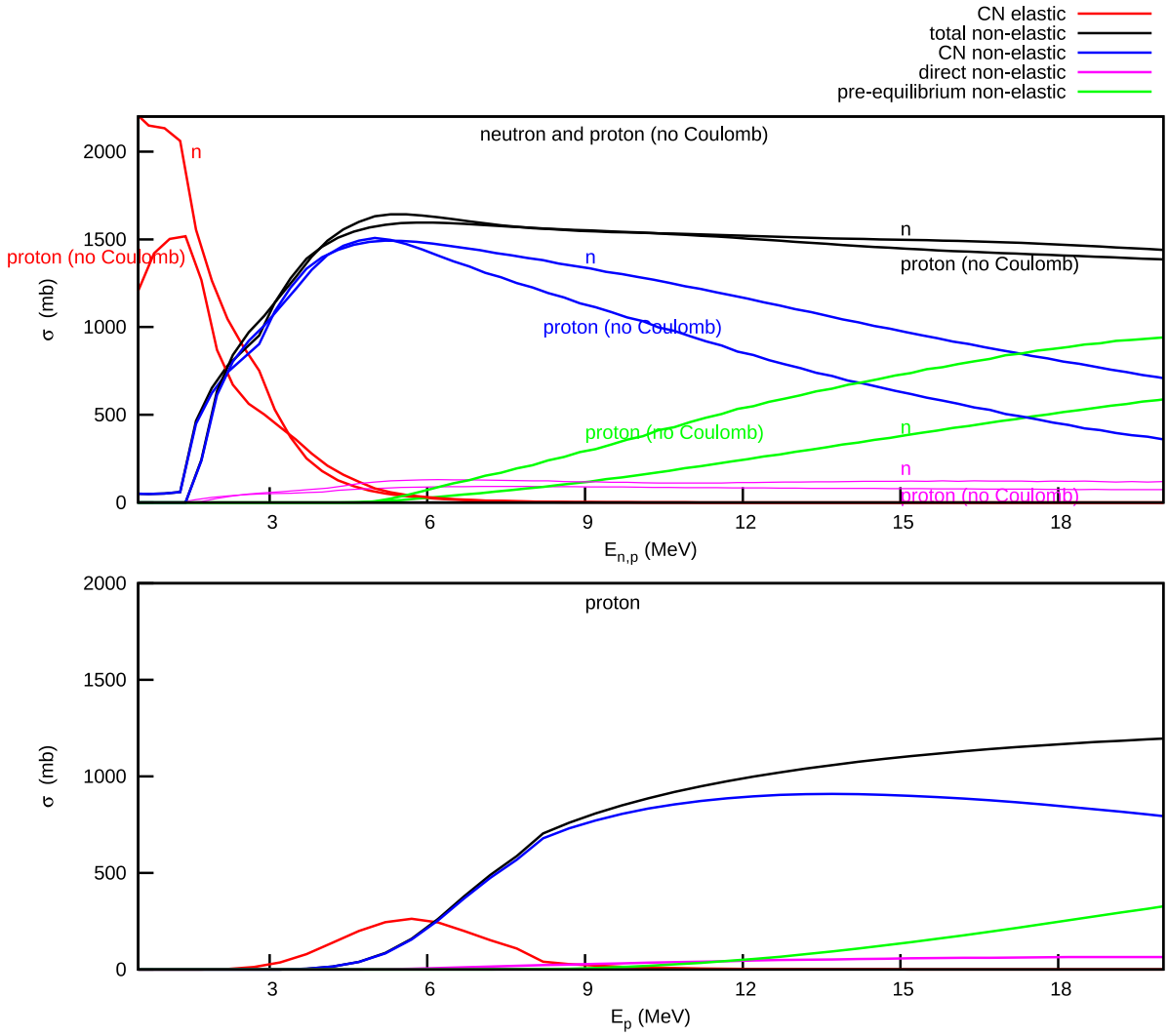

FIG. 9. To illustrate the dominant role played by the electromagnetic interaction in generating the differences between the neutron and proton reactions, we plot here the contribution of each reaction mechanism to the nonelastic/reaction cross section for a neutron, a proton, and a proton with no Coulomb barrier projectile on a ^{58}Ni target. We employed the TALYS 1.9 default settings to extract the theoretical curves for the first two projectiles. For the "proton (no Coulomb)" case we simply removed the Coulomb term from the proton-^{58}Ni OMP, hence switching off the electromagnetic interaction in the incoming channel. The "total nonelastic" curve does not include the CN elastic contribution (i.e., it is the reaction cross section minus the CN elastic contribution); hence, it is simply the sum of the CN, direct, and preequilibrium nonelastic cross section values shown here.

$8999.2 - 3418.6 = 5580.6$ keV; the CN decay depends on the available excitation energy, therefore the difference mentioned above is a typical concern within our paper; the neutron and proton reactions populate however relatively high excitation energies, in the continuum, where statistical approaches are used to describe the CN formation and its decay; this, in fact, diminishes the impact of the level scheme difference between ^{59}Ni and ^{59}Cu.

(3) The fact that ^{58}Ni has two extra neutrons as compared to protons generates a different number of CN excitons that can be created when describing the preequilibrium reactions; this is probably the main reason for the difference seen in Fig. 9 between the proton (no Coulomb) and neutron preequilibrium contributions.

(4) Nucleon OMP-related: all V_V, W_V... potential well depths have a $(E - E_f)$ energy dependence; this translates into a different energy dependence of the OMP because the Fermi energy, E_f, is different in the neutron (-10.61 MeV) and proton (-5.79 MeV) cases [see relations (4.5) and (4.6) from the TALYS 1.9 User Manual [35]].

(5) Nuclear structure-induced: the two CN through which the neutron and proton reactions proceed are different.

(6) Isospin-dependent terms in the optical potential: even without the electromagnetic interaction, the neutron and proton are not identical.

In terms of their phenomenological OMPs mentioned above, there are only two formal differences between the neutron and proton cases: the additional Coulomb term V_C for protons and the opposite sign of the Lane term [33–35]. These similarities were exploited in the present paper to relate the neutron and proton inelastic channels. The neutron

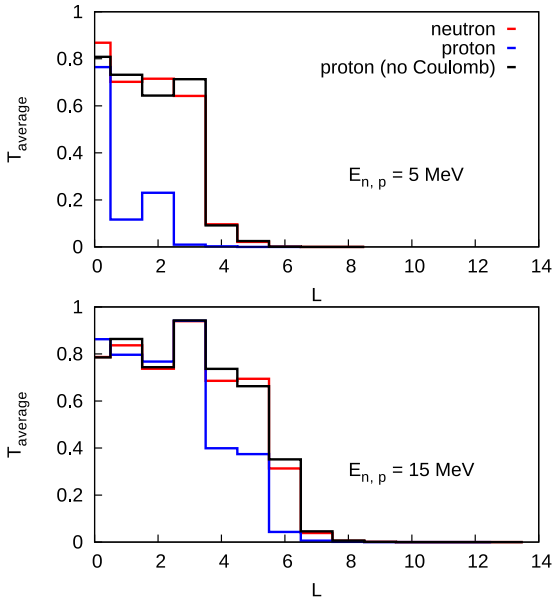

FIG. 10. The CN transmission coefficients of the neutron and proton fluxes at 5 (top panel) and 15 MeV (bottom panel) as a function of the orbital angular momentum L for a ^{58}Ni target, according to TALYS 1.9. The additional proton (no Coulomb) calculation was performed using an incident proton with no Coulomb barrier to illustrate its impact on the observables populated in the compound nucleus.

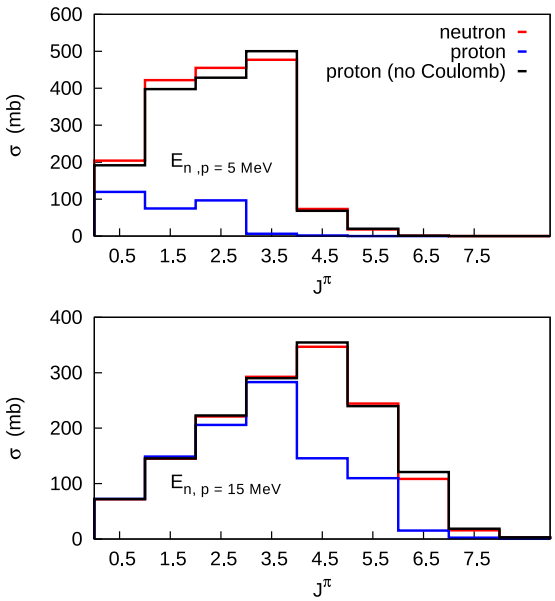

FIG. 11. The total angular momentum and parity J^{π} populated in the CN by 5- (top panel) and 15-MeV (bottom panel) nucleons incident on a ^{58}Ni target, according to TALYS 1.9. The proton (no Coulomb) calculation is the same as in Fig. 10. For all calculations, the code's output consists of separate angular momenta values for the negative and the positive parity states; hence, we simply added the two to obtain the values plotted here.

optical potential extracted in this way, which in the following we will call *n*-inferred, uses an identical parametrization and Lane term to the proton ones but no Coulomb barrier. Details regarding this point are given in Secs. V B and V C. We emphasize however that the *n*-inferred optical potential, and the subsequent inelastic cross sections calculated using it, was determined in a manner *independent* of the neutron experimental data (only proton data were used to tune the parametrization).

The optical model calculation provides, among other quantities, transmission coefficients and spin and parity population in the CN. One relevant issue for the present paper is the mismatch between the most important observables being populated in the neutron and proton cases as the subsequent statistical model calculation strongly depends on these observables.

Figure 9 shows the contribution of each reaction mechanism as a function of incident energy for the neutron, proton, and proton (no Coulomb) cases, according to TALYS 1.9. The proton (no Coulomb) calculation shows to some degree the magnitude of the residual difference between the neutron and proton reactions if the electromagnetic interaction is switched off in the incoming channel. It is remarkable how similar the neutron and proton (no Coulomb) cases are: see, for example, the direct contribution and the total nonelastic cross section. There are, however, important differences below 6 MeV. Even though the compound nonelastic and pre-equilibrium contributions are very different in the two cases, they add up (together with the almost identical direct contributions) to a very similar nonelastic cross section. It is not clear to us what is the cause for the different CN elastic contributions below 3-MeV incident energy in the neutron and proton (no Coulomb) cases but this difference seems to be correlated with the CN nonelastic contributions in the same region.

Figure 10 displays the transmission coefficients of the incident neutron, proton, and proton (no Coulomb) fluxes inside the CN. The neutron and proton (no Coulomb) transmission coefficients have very similar values, which means that, if one neglects the electromagnetic interaction, the absorbed flux is practically the same in the neutron and proton cases. The remaining difference progressively diminishes at higher incident energies. Such electromagnetic effects are to be expected considering that the Coulomb term V_C of the proton (no Coulomb) optical potential is not rigorously set to zero within our calculations. We simply increase by a factor 1000 the reduced Coulomb radius r_C which, in turn, reduces (almost) to zero the V_C contribution [see expression (4.4) of the TALYS 1.9 User Manual [35]].

Figure 11 displays the total angular momentum and parity populated in the CN for the neutron, proton, and proton (no Coulomb) cases, according to TALYS 1.9. At both incident energies, the neutron and proton (no Coulomb) projectiles populate almost identical values, proving important similarities between the two cases (at least) at the optical model stage of the calculation. The remaining difference might be generated by electromagnetic effects (as for the CN transmission coefficients).

B. Results for ^{58}Ni using phenomenological nucleon OMPs

We mention that all the results discussed in this section were obtained using global neutron and proton OMPs (even though TALYS 1.9 also offers the option of local nucleon potentials for ^{58}Ni [35]).

In Ref. [22] we describe a procedure able to relate with reasonable precision the neutron and proton inelastic channels on ^{16}O and ^{28}Si. It consists mainly of three steps: (i) measure the proton-induced inelastic cross sections, (ii) tune the reaction calculations aiming to describe as precisely as possible these cross sections, and (iii) infer a proton-based neutron potential. For validation, the proton-based neutron inelastic cross sections calculated using this potential are then compared with the data measured at GELINA.

The study undertaken in Ref. [22] has however several issues difficult to address—mostly electromagnetic effects generated by the removal of the Coulomb term V_C from the proton OMP. Because of this fact, we explore here a different approach to this problem. It consists in essence of fixing the parametrization for the proton potential using the proton data measured at the Tandem Accelerator of IFIN-HH and, then, transferring the same parameters also to the *n*-inferred calculation.

The Lane term of the optical potential was introduced to take into account the (very small) difference generated by the isospin asymmetry between the neutron and proton projectiles [33,34]. With this in mind, we mention that the tuning of the proton-default calculations was performed by modifying only the asymmetry parameter $21(N-Z)/A$ corresponding to the isospin-dependent term of the potential (see Table 4.2 from the TALYS 1.9 User Manual [35]). We performed the parameter changes in a transition-by-transition basis ending up with a 32%, 11%, and 12% decrease of the global (default) value of this term for the 1454.2-, 1004.8- and 1321.2-keV transitions, respectively. For the 1454.2- and 1004.8-keV γ rays, only such changes were needed to improve the agreement with the measured proton data. For the 1321.2-keV transition however this was not enough as the TALYS default calculation greatly overestimates the experiment (see Figs. 7 and 8). Consequently, in this case we also had to decrease by 55% the diffuseness a_V of the real part of the global (default) proton OMP [35]. The effect of this parameter tuning can be seen in Fig. 12 for the main three transitions in ^{58}Ni.

The same figure also displays the results of our study aiming to relate the neutron and proton inelastic channels (see the *n*-inferred curves). We point out again that these curves were obtained in a manner independent of the neutron data. We used the experimental values for the proton-induced inelastic channel to fix the parametrization of the nucleon optical potential and we employed the same proton-based parameters in a subsequent neutron $+^{58}$ Ni calculation. One can see that in all three cases the *n*-inferred curve is able to describe a little better the neutron experimental data as compared to the neutron-default calculation (particularly the low energy region of the 1454.2- and 1321.2-keV transitions). Unfortunately, we are still unable to reasonably describe the cross section plateau clearly seen at intermediate energy on the neutron data for the 1454.2- and 1004.8-keV γ rays. This shows the limitations of the current nucleon-^{58}Ni optical potential (as already commented in Sec. IV).

C. Results for ^{58}Ni using semimicroscopical nucleon OMPs

This section shows our results for the 1454.2-, 1004.8-, and 1321.2-keV transitions in ^{58}Ni using the semimicroscopical nucleon OMP of Bauge *et al.* [33–35,58]. Similarly to the previous section, the tuned proton and *n*-inferred calculations consisted of modifying proton default JLM parameters and then using the same parameters also in the neutron calculation, respectively. More precisely, to improve the agreement with the experimental data, we modified the proton l_V, l_W, and l_{W1} potential normalization factors which are multiplied with the nuclear matter asymmetry parameter $\alpha = (\rho_n - \rho_p)/\rho$ in the expression of the JLM potential [see relations (6) and (7) of Ref. [58] and, also, the TALYS 1.9 User Manual [35]]. This expression for the nuclear matter asymmetry parameter is a microscopical form while an averaged form $\alpha = (N-Z)/A$ can also be used (see Sec. V.A of Ref. [58]). Therefore, by tuning on the $\alpha = (\rho_n - \rho_p)/\rho$ form of the nuclear matter asymmetry, we are essentially mimicking what we did in the previous section but at a more microscopical level. Also in this case we performed the changes in a transition-by-transition basis ending up with the following tuned values.

(1) For the 1454-keV transition, l_V was decreased by 46%.

(2 For the 1004-keV transition, l_{W1} was decreased by 87%.

(3) For the 1321-keV transition, both l_V and l_W were decreased by 87% and 16%, respectively.

The results of these parameter changes can be seen in Fig. 13. We first note that the semimicroscopical "TALYS JLM default (n, n')" calculation performs better in describing the neutron data as compared to the "TALYS default (n, n')" curves shown in Fig. 12 which employed standard OMP, except for the 1454.2-keV γ ray where it overestimates the experimental values in the 7–11-MeV incident energy range. In general, the *n*-inferred curves describe better the data measured at GELINA as compared to the neutron JLM default calculation (see especially the case of the 1454.2-keV transition). Unfortunately, this is not the case for the 1321.2-keV γ ray where the *n*-inferred curve overestimates the threshold region even though it shows small improvements in the remaining incident energy range. This is the only example where the *n*-inferred calculation performs worse than the default case. Comparisons for other ^{58}Ni transitions would have been helpful but, as mentioned, in the proton-induced experiment we were not able to extract clean cross sections for additional γ rays.

It is important to point out that the improved agreement with the neutron data shown by the *n*-inferred calculation happens only *after* the default proton optical model potential is tuned on proton experimental data (this is also the case for the results discussed in Sec. V B). This indicates both the level of Lane consistency of the nucleon OMP implemented in reaction codes like TALYS and also that the isospin symmetry can, to some extent, be exploited to extract neutron inelastic cross sections by performing only proton-induced experiments.

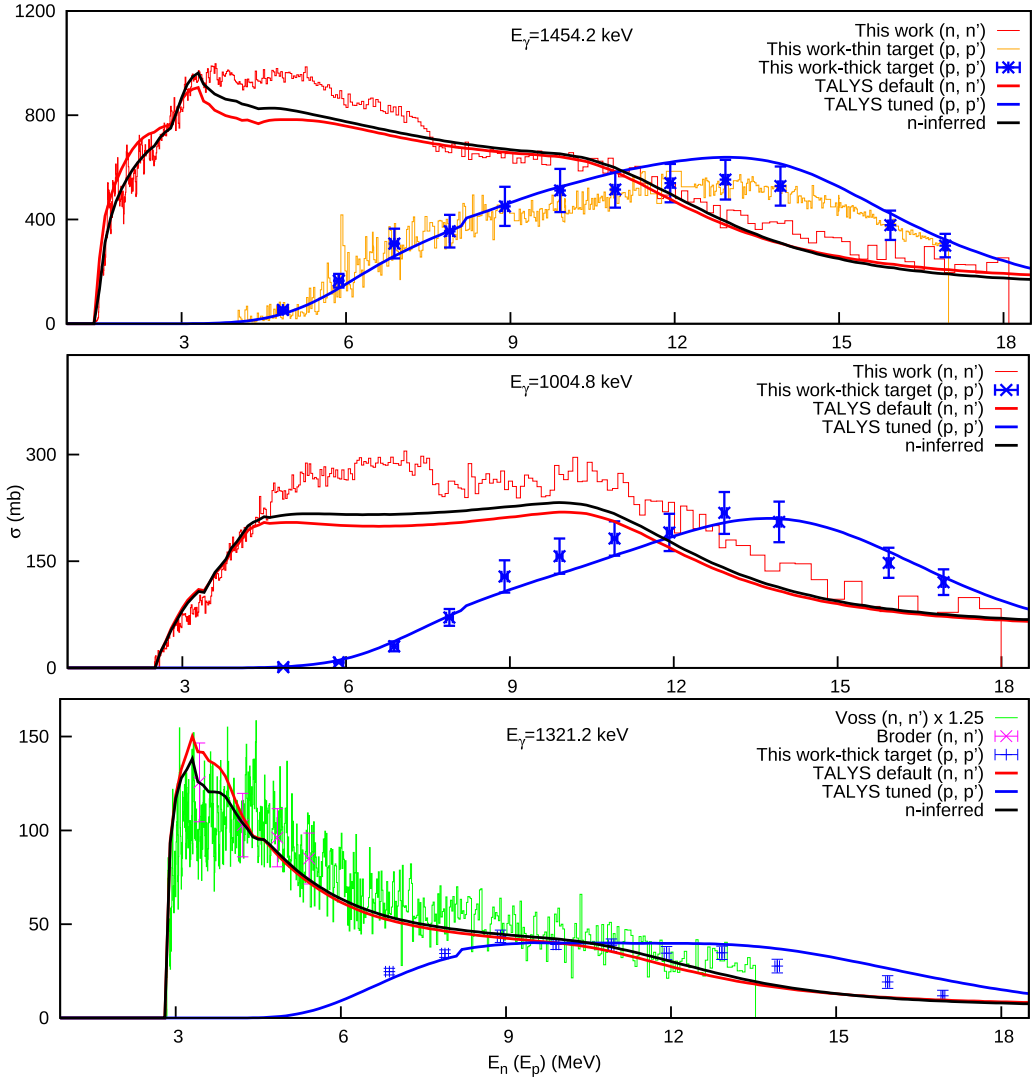

FIG. 12. The results of the present paper for the main three transitions in ^{58}Ni using the standard neutron and proton OMPs. The Voss *et al.* [15] data are the same as in Fig. 8. For the 1454.2- and 1004.8-keV transitions, the "TALYS tuned (p, p')" calculation only involved changes of the default value for the asymmetry parameter associated with the Lane term. This was not the case for the last transition, which required additional modifications also of the diffuseness a_V for a better description of the proton data. The curves associated with the "n-inferred" calculation were obtained as explained in the main text.

D. Discussion

As described in the previous two sections, the nucleon OMP parameter tuning reported in the present paper involved indeed huge changes of the default values for both standard and semimicroscopical/JLM potentials. However, such modifications are to be expected when considering the very small strength of the isospin-dependent term in the OMP (after all the nucleon isospin asymmetry is very small). This is especially true in those cases where the proton default calculation is very far from the experimental data. The magnitude of the required changes also points to the poor quality of the nucleon OMP itself in this mass region and/or, most likely, to other poorly known reaction ingredients that TALYS calls during the calculation.

Unfortunately, despite the progress already made, a number of issues still have to be addressed when aiming to relate the neutron and proton inelastic channels. As we showed, at least at the OMP level of the reaction calculation and if one removes the Coulomb interaction, the two reactions behave very similarly: practically all the observables given by the initial OMP calculation have fairly close values. However, all of these are *reaction*-related ingredients and are not *structural*. The differences induced by the latter start to manifest when structure information is imported by TALYS from the RIPL database [59]: nuclear masses, deformation parameters, neutron and proton separation energies, etc. Consequently, the two reactions imply the modeling of different, nonmirror, compound nuclei (^{59}Ni versus ^{59}Cu) within the Hauser-Feshbach and the exciton models for CN and preequilibrium reactions, respectively, while starting from a 5580.6-keV difference between their associated excitation energy grids. Indeed, these facts play a role in the differences we observe in Fig. 9 between the two reactions.

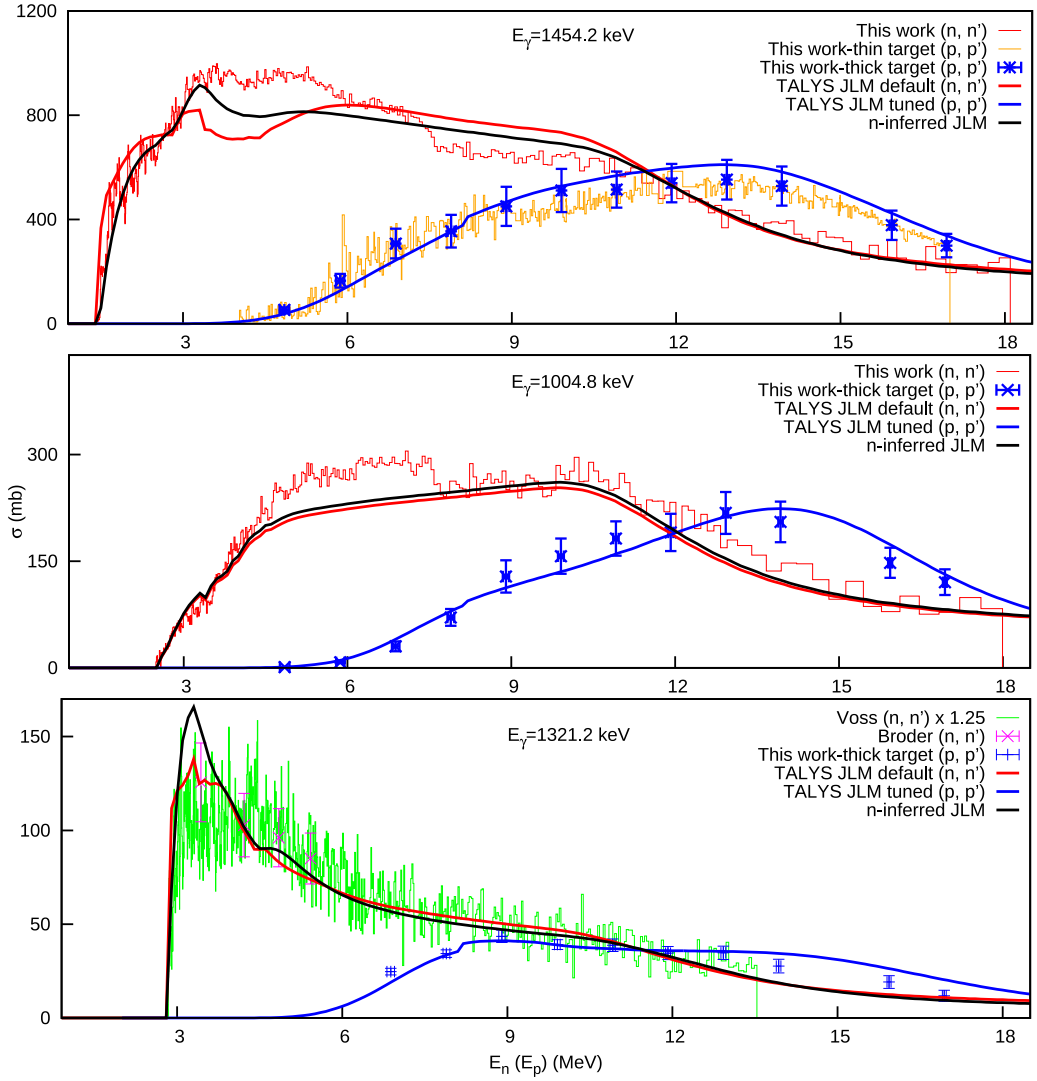

FIG. 13. The results of the present paper for the main three transitions in ^{58}Ni using the semimicroscopical (JLM) nucleon OMP. The Voss *et al.* [15] data are the same as in Fig. 8. The TALYS tuned (p, p') calculation involved modifications of the l_V, l_W, and l_{W1} JLM potential normalization factors, which are multiplied with the nuclear matter asymmetry parameter α in the expression of this potential [35,58]. The curves associated with the *n*-inferred calculation were obtained similarly to the corresponding ones from Fig. 12.

We note that within the present paper one fixes the parametrization for the nucleon-target OMP using *only* the experimental constraints offered by the inelastic channel, while then exploiting the Lane consistency of this potential to relate the neutron and proton cases. However, a more rigorous approach would be to first maximize the Lane consistency of the potential via tuning not only on inelastic data but also on elastic and quasielastic [(p, n) reactions to Isobaric Analogue States] data. Such an approach was undertaken in Refs. [60,61] for the elastic channel in the case of several nuclei, including ^{58}Ni. By exploiting the Lane consistency of the nucleon-target potential, the authors inferred neutron elastic angular distributions from proton ones making use only of proton-induced data (elastic and quasielastic) and reaction calculations, hence proving that the neutron and proton elastic channels can be related with high precision. Therefore, maximizing the Lane consistency of the nucleon OMP by first reproducing the results of Refs. [60,61] for the elastic channel would be indeed helpful in our own investigation dedicated to a more complicated case study: the inelastic channel. The inelastic is more complicated as compared to elastic because, among other reasons, one also needs to correctly model what happens to the absorbed incident flux in the CN (Hauser-Feshbach, excitons, increased nuclear structure sensitivity, etc). If we are to take such an approach, it will require measuring, in addition to proton inelastic data, also proton elastic and quasielastic angular distributions.

However, making use of the elastic channel in this way might not be a sufficiently stringent constraint for the nucleon OMP. In this respect, Pruitt *et al.* [62] performed an extensive optical model analysis for several nuclei, including ^{16}O, ^{58}Ni, and ^{40}Ca of interest for our group, and made some interesting findings. They showed that tuning the neutron and proton

elastic angular distributions was not a very stringent constraint for all-important imaginary (absorptive) terms of the potential and, in particular, for clarifying its nuclear asymmetry dependence. For better results, a simultaneous analysis of several types of neutron and proton data must be performed [62]. As we hope to maximize the Lane consistency of the nucleon optical potential via fitting on elastic data (and, in doing so, to also describe more precisely the part of the incident flux being absorbed in the CN), such findings are relevant to our investigation. Pruitt *et al.* used a nonlocal, dispersive optical model potential that extends both below and above the Fermi energy and which has "Lane-like" dependencies for asymmetrical nuclei [see expressions (A.15–A.18) of Ref. [62]]. This is not the case for the nucleon OMP used in the present paper which is a local, positive-energy-only potential [35]. The nonlocal character allows for structural data, like charge densities and binding energies, to constrain the potential above the Fermi energy, and for elastic, reaction, and total cross section data to constrain the potential below this energy (hence coupling scattering data with nuclear structure quantities). Pruitt *et al.* concluded that assuming a nonlocal dependence of the potential was actually crucial in obtaining a quality fit of the neutron and proton data. Because relating the neutron and proton inelastic channels also depends on nuclear-structure-induced differences, using such nonlocal potentials may be more helpful in understanding these differences. However, this type of issue deserves a future in-depth investigation.

We end this section with the observation that all the changes discussed in this paper of the default neutron and proton potentials will make them behave more similarly and, consequently, these modifications should ideally improve the agreement between the neutron and proton cross sections across reaction channels, in particular, also for the inelastic. We emphasize however that the similarities between the two nucleons will stop at the level where the isospin symmetry stops. A systematic study of several target isospins might therefore reveal new aspects with regard to the nucleon-target OMPs presently used to model these reactions and, in particular, about the (possible) isospin-breaking terms of these potentials.

VI. CONCLUSIONS

This paper reports measurements of neutron- and proton-induced inelastic scattering cross sections on ^{58,60,64}Ni measured at the GELINA neutron source of EC-JRC-Geel using the GAINS spectrometer and at the 9-MV Tandem Accelerator of IFIN-HH-Bucharest. The angle-integrated γ-production inelastic cross sections for several transitions are reported (with an uncertainty smaller than 4–6% for the most intense γ rays) and compared with other experimental data and with TALYS 1.9 default calculations. This comparison shows several limitations of the default nucleon-target OMP for these nickel isotopes.

The last part of this paper presents a comparison of the neutron and proton inelastic cross sections with the purpose of studying to what extent the two reaction channels can be related. We show that—using the constraints offered by proton experimental data and exploiting the Lane consistency of the nucleon OMPs—one can infer a neutron optical potential that better describes the neutron data measured at GELINA, as compared to the default calculation. These results are extensively discussed in the last section of the paper, which also presents the remaining issues of our approach together with future plans for mitigation. We report encouraging results suitable for further improvement.

ACKNOWLEDGMENTS

The work was supported by the European Commission's Seventh Framework Programme Fission-2013-CHANDA (Project No. 605203) and by the Romanian Ministry of Research, Innovation, and Digitization, CNCS/CCCDI-UEFISCDI, through Projects No. PN-III-P4-ID-PCE-2016-0025 and No. PN-III-P1-1.1-TE-2019-0337, within PNCDI III. This project has also received funding from the Euratom research and training program 2014–2018 under Grant No. 847552 (SANDA). We would like to thank the Institut de Radioprotection et de Sûreté Nucléaire (IRSN) for providing financial support for sample acquisition under Grants No. JRC-3465 and No. LS20361. We would further like to acknowledge the support team of the GELINA facility for providing good working conditions during the neutron experiment, and we are also very grateful to the 9-MV Tandem Accelerator of IFIN-HH operators for their dedication shown during the very demanding (p, p') measurement.

[1] E. M. Hussein, Physics Open **5**, 100038 (2020).
[2] D. T. Ingersoll, Prog. Nucl. Energy **51**, 589 (2009).
[3] https://www.gen-4.org.
[4] C. D. Bowman III *et al.*, Nucl. Instrum. Methods Phys. Res., Sect. A **320**, 336 (1992).
[5] C. Rubbia, AIP Conf. Proc. **346**, 44 (1995).
[6] C. D. Bowman, Annu. Rev. Nucl. Part. Sci. **48**, 505 (1998)
[7] https://www-pub.iaea.org/MTCD/Publications/PDF/TE-1766_web.pdf.
[8] B. Raj, U. Kamachi Mudali, M. Vijayalakshmi, M. D. Mathew, A. K. Bhaduri, P. Chellapandi, S. Venugopal, C. S. Sundar, B. P. C. Rao, and B. Venkataraman, Adv. Mat. Res. **794**, 3 (2013).
[9] J. Meija, T. B. Coplen, M. Berglung, W. A. Brand, P. De Bievre, M. Groning, N. E. Holden, J. Irrgeher, R. D. Loss, T. Walczyk, and T. Prohaska, Pure Appl. Chem. **88**, 293 (2016).
[10] N. Otuka *et al.*, Nucl. Data Sheets **120**, 272 (2014).
[11] D. A. Bazavov, I. E. Kashuba, V. P. Prikhod'ko, A. A. Golubova, and S. V. Stoljarov, Ukr. Fiz. Zh. **28**, 1791 (1983).
[12] D. L. Broder, V. E. Kolesov, A. I. Lashuk, I. P. Sadokhin, and A. G. Dovbenko, Sov. Atomic Energy **16**, 113 (1964).

[13] E. S. Konobeevskii, R. M. Musaelyan, V. I. Popov, and I. V. Surkova, Bull. Russ. Acad. Sci. - Phys. **35**, 2127 (1972).

[14] G. Tessler and S. Glickstein, in *Proceedings of the Conference on Nuclear Cross Sections and Technology*, edited by R. A. Schrack and C. D. Bowman (Center for Radiation Research National Bureau of Standards, Washington, D.C., 1975), Vol. 2, p. 934.

[15] F. Voss, S. Cierjacks, D. Erbe, and G. Scmalz, in *Proceedings of the Conference on Nuclear Cross Sections and Technology*, edited by R. A. Schrack and C. D. Bowman (Center for Radiation Research National Bureau of Standards, Washington, D.C., 1975), p. 916.

[16] K. Nishimura *et al.*, Nucl. Phys. **70**, 421 (1965).

[17] S. Traiforos *et al.*, Nucl. Sci. Eng. **72**, 191 (1979).

[18] W. Breunlich *et al.*, Z. Naturforsch. **26**, 451 (1971).

[19] N. Fotiades, M. Devlin, R. C. Haight, R. O. Nelson, S. Kunieda, and T. Kawano, Phys. Rev. C **91**, 064614 (2015).

[20] A. Negret *et al.*, Phys. Rev. C **88**, 034604 (2013).

[21] M. Boromiza, Nucleon inelastic scattering cross sections on ^{16}O and ^{28}Si, Ph.D. thesis, University of Bucharest, 2018.

[22] M. Boromiza *et al.*, Phys. Rev. C **101**, 024604 (2020).

[23] J. E. Escher, J. T. Harke, F. S. Dietrich, N. D. Scielzo, I. J. Thompson, and W. Younes, Rev. Mod. Phys. **84**, 353 (2012).

[24] A. Bohr and B. Mottelson, *Nuclear Structure* (World Scientific, Singapore, 1998).

[25] C. Plettner *et al.*, Phys. Rev. C **71**, 051602(R) (2005).

[26] J. T. Burke *et al.*, Phys. Rev. C **73**, 054604 (2006).

[27] B. L. Goldblum, S. G. Prussin, U. Agvaanluvsan, L. A. Bernstein, D. L. Bleuel, W. Younes, and M. Guttormsen, Phys. Rev. C **78**, 064606 (2008).

[28] M. Petit *et al.*, Nucl. Phys. A **735**, 345 (2004).

[29] S. Boyer *et al.*, Nucl. Phys. A **775**, 175 (2006).

[30] J. M. Allmond *et al.*, Phys. Rev. C **79**, 054610 (2009).

[31] S. Chiba and O. Iwamoto, Phys. Rev. C **81**, 044604 (2010).

[32] B. Pandey *et al.*, Phys. Rev. C **93**, 021602(R) (2016).

[33] A. Lane, Nucl. Phys. **35**, 676 (1962).

[34] A. Lane, Phys. Rev. Lett. **8**, 171 (1962).

[35] A. Koning, S. Hilaire, and M. Duijvestijn, in *Proceedings of the International Conference on Nuclear Data for Science and Technology*, edited by O. Bersillon, F. Gunsing, E. Bauge, R. Jacqmin, and S. Leray (EDP Sciences, 2007), Vol. 211, p. 1.

[36] W. Mondelaers and P. Schillebeeckx, Notiziario Neutroni e Luci di Sincrotrone **11**, 19 (2006).

[37] D. Deleanu, C. Borcea, P. Dessagne, M. Kerveno, A. Negret, A. J. M. Plompen, and J. C. Thiry, Nucl. Instrum. Methods Phys. Res., Sect. A **624**, 130 (2010).

[38] Acqiris manual, http://literature.cdn.keysight.com/litweb/pdf/U1092-90005.pdf.

[39] C. Rouki *et al.*, Nucl. Instrum. Methods Phys. Res. A **672**, 82 (2012).

[40] A. Olacel, C. Borcea, P. Dessagne, M. Kerveno, A. Negret, and A. J. M. Plompen, Phys. Rev. C **90**, 034603 (2014).

[41] A. Olacel, C. Borcea, M. Boromiza, P. Dessagne, G. Henning, M. Kerveno, L. Leal, A. Negret, M. Nyman, and A. J. M. Plompen, Eur. Phys. J. A **54**, 183 (2018).

[42] D. Bucurescu, G. Cata-Danil, and N. V. Zamfir, Nuclear Physics News **17**, 5 (2007).

[43] D. G. Ghita *et al.*, AIP Conf. Proc. **1525**, 208 (2013).

[44] http://faster.in2p3.fr/index.php/introduction/hardware/daughter-boards/18-mosahr.

[45] M. Boromiza, C. Borcea, A. Negret, A. Olacel, and G. Suliman, Nucl. Instrum. Methods Phys. Res. A **863**, 15 (2017).

[46] L. Stoica, Dead time corrections for proton inelastic cross section measurements, Bachelor thesis, University of Bucharest, 2020.

[47] L. C. Mihailescu, C. Borcea, and A. J. M. Plompen, Nucl. Instrum. Methods Phys. Res. A **578**, 298 (2007).

[48] L. C. Mihailescu, Neutron (n, x$n\gamma$) cross sections measurements for ^{52}Cr, ^{209}Bi and ^{206,207,208}Pb from threshold up to 20 MeV, Ph.D. thesis, European Commission Joint Research Center Geel, 2006.

[49] A. Carlson *et al.*, Nucl. Data Sheets **110**, 3215 (2009).

[50] K. E. Atkinson, *An Introduction to Numerical Analysis* (Wiley, New York, 1989).

[51] M. Boromiza *et al.*, Proton inelastic scattering cross section measurements on ^{16}O and ^{28}Si, in *Proceedings of the International Conference on Nuclear Data for Science and Technology* (EDP Sciences, 2017), Vol. 146, p. 11015.

[52] C. Nesaraja, S. Geraedts, and B. Singh, Nucl. Data Sheets **111**, 897 (2010).

[53] M. Kerveno *et al.*, Phys. Rev. C **104**, 044605 (2021).

[54] A. Olacel *et al.*, Neutron inelastic cross section measurements on ^{58}Ni and ^{60}Ni, in *Proceedings of the International Conference on Nuclear Data for Science and Technology* (EDP Sciences, 2020), Vol. 239, p. 01040.

[55] X-6 Monte Carlo Team, MCNP—A general N-particle transport code, version 6, Volume I: Overview and theory, Los Alamos National Laboratory, Los Alamos, NM, http://laws.lanl.gov/vhosts/mcnp.lanl.gov.

[56] B. V. Carlson, The optical model, in *Proceedings of the Joint ICTP-IAEA Workshop on Nuclear Reaction Data for Advanced Reactor Technologies*, 2010 (unpublished).

[57] A. de Shalit and H. Feshbach, *Theoretical Nuclear Physics, Volume 1: Nuclear Structure* (Wiley, New York, 1974).

[58] E. Bauge, J. P. Delaroche, and M. Girod, Phys. Rev. C **63**, 024607 (2001).

[59] R. Capote *et al.*, Nucl. Data Sheets **110**, 3107 (2009).

[60] J. Carlson, D. Lind, and C. Zafiratos, Phys. Rev. Lett. **30**, 99 (1973).

[61] J. Carlson, C. Zafiratos, and D. Lind, Nucl. Phys. A **249**, 29 (1975).

[62] C. D. Pruitt *et al.*, Phys. Rev. C **102**, 034601 (2020)